

Ultra-Stable and Robust Response to X-Rays in 2D Layered Perovskite Micro-Crystalline Films Directly Deposited on Flexible Substrate

Ferdinand Lédée, Andrea Ciavatti,* Matteo Verdi, Laura Basiricò, and Beatrice Fraboni

2D layered hybrid perovskites have recently attracted an increasing interest as active layers in LEDs and UV–Vis photodetectors. 2D perovskites crystallize in a natural self-assembled quantum well-like structure and possess several interesting features among which low-temperature (<100 °C) synthesis and low defect density. Here are presented solid-state ionizing radiation direct detectors based on the 2D layered hybrid perovskite $\text{PEA}_2\text{PbBr}_4$ ($\text{PEA} = \text{C}_6\text{H}_5\text{C}_2\text{H}_4\text{NH}_3^+$) deposited from solution using scalable techniques and directly integrated onto a pre-patterned flexible substrate in the form of micro-crystalline films displaying crystal-like behavior, as evidenced by the ultra-fast (sub-microsecond) and good detection performances under UV light. The effective detection of X-rays (up to 150 kVp) is demonstrated with sensitivity values up to $806 \mu\text{C Gy}^{-1} \text{cm}^{-2}$ and Limit of Detection of 42nGy s^{-1} , thus combining the excellent performance for two relevant figures of merit for solid-state detectors. Additionally, the tested devices exhibit exceptionally stable response under constant irradiation and bias, assessing the material robustness and the intimate electrical contact with the electrodes. $\text{PEA}_2\text{PbBr}_4$ micro-crystalline films directly grown on flexible pre-patterned substrate open the way for large-area solid-state detectors working at low radiation flux for ultra-fast X-ray imaging and dosimetry.

the last decade. In particular, the development of light and flexible devices would represent a major breakthrough in the field, as it allows new detector design and applications, for example, portable real-time X-ray dosimeters or curved digital X-ray imagers.^[1] Exposure to high doses of X-rays increases the risks of developing radiation-induced disorders such as cancers^[2] and enhancing the detection limit of detectors is a critical key issue for medical application, since it would help reducing the radiation dose delivered to the patient and therefore limit the radiation hazards linked to radiation therapy and diagnostics (e.g., mammography, X-ray tomography). The specifications cited above call for the development of solution-processable X-ray direct detecting materials compatible with low-temperature deposition on flexible plastic substrates, and in addition capable of working at low radiation doses. Nonetheless, all these requirements cannot be easily met with a single material due to the dual necessity of low mechanical stiffness

1. Introduction

Solid-state direct X-ray detectors are crucial in a wide range of application such as medical radiography, nuclear, and civil security. As opposed to the presently available thick and rigid solid-state X-ray sensors, the demand for low-cost, sensitive, and possibly lightweight detectors has grown extensively during


and high X-ray absorption, the latter being usually achieved by thick and heavy absorbing layers.

Indeed, traditional state-of-the-art materials involved in direct X-ray detection include silicon (Si), amorphous Selenium ($\alpha\text{-Se}$), and Cadmium Zinc Telluride (CZT), which are known for their high X-ray stopping power owing to their high atomic number (Z) and density. Flexible applications are however hindered by their high processing temperature incompatible with plastic substrates and their mechanical stiffness. Recently, organic semiconductors have appeared as promising alternatives to traditional inorganic semiconductors for direct X-ray detection.^[3,4] Organic semiconductors possess appealing properties, in particular, the possibility to process them via large-area solution-based techniques such as bar-coating^[5] or inkjet printing^[6] onto flexible substrates. The low Z of organic materials however limits their stopping power, restraining the detection of high-energy X-rays at low radiation doses. The trade-off between mechanical rigidity and large X-ray absorption thus represents an interesting challenge to tackle for the development of novel X-ray detecting materials.

In the past few years, the research on new materials for direct X-ray detection has largely revolved around hybrid organic/inorganic halide perovskites (HOIPs). 3D HOIPs with composition

F. Lédée, A. Ciavatti, M. Verdi, L. Basiricò, B. Fraboni
Department of Physics and Astronomy
University of Bologna
Viale Berti Pichat 6/2, Bologna 40127, Italy
E-mail: andrea.ciavatti2@unibo.it

A. Ciavatti, M. Verdi, L. Basiricò, B. Fraboni
National Institute for Nuclear Physics – INFN section of Bologna
Viale Berti-Pichat 6/2, Bologna 40127, Italy

 The ORCID identification number(s) for the author(s) of this article can be found under <https://doi.org/10.1002/adom.202101145>.

© 2021 The Authors. Advanced Optical Materials published by Wiley-VCH GmbH. This is an open access article under the terms of the Creative Commons Attribution License, which permits use, distribution and reproduction in any medium, provided the original work is properly cited.

DOI: 10.1002/adom.202101145

ABX_3 ($A = Cs^+$, $CH_3NH_3^+$, $CH(NH_2)NH_2^+$; $B = Pb^{2+}$, Sn^{2+} ; $X = I^-$, Br^- , Cl^-) have demonstrated very good performances as X-rays detectors, exhibiting mobility-lifetime ($\mu\tau$) products, and X-ray absorption coefficients similar to that of CZT.^[7–9] Their most notable asset is however represented by their good processability, which allows to obtain centimetre-scale single crystal with trap state densities in the order of 10^9 cm^{-3} using solution-based techniques at low temperature ($<100\text{ }^\circ\text{C}$).^[10,11] On the one hand HOIPs detectors based on polycrystalline morphologies exhibit fairly good performances,^[12–17] however they are limited by lower bulk resistivity,^[18] higher trap states density,^[9] and significant ion migration effects leading to large dark current drift^[19] with respect to HOIPs detectors based on single crystals.^[11,20,21] Briefly, single crystal-based devices suffer from the difficulty to produce large-area pixelated detectors directly integrated onto read-out electronics, and therefore showing a lack of scalability. Polycrystalline films are thus extremely promising candidates to envisage large area technology implementation.

Very recently, low-dimensional perovskites have attracted a renewed interest in the fields of LEDs and UV–Vis photo-detectors.^[22,23] These perovskites are represented by the general formula $(R-NH_3)_2A_{n-1}B_nX_{3n+1}$ with $n = 1, 2, 3, \dots$, where R is an alkyl or aryl group. Low-dimensional perovskites are characterized by a layered crystal structure in which corner-shared BX_6 octahedra sheets are intercalated between bilayers of $R-NH_3^+$ organic spacers. Their electronic structure is akin to a multiple quantum well where the inorganic layers constitute the wells and the organic spacers the barriers. For $n = 1$, the perovskite formula is $(R-NH_3)_2PbX_4$ and the BX_4^{2-} sublattice organizes in purely 2D planar monolayers. Due to the high dielectric contrast between the organic and inorganic moieties, the charge carriers are strongly confined in the inorganic layers and 2D HOIPs present large exciton binding energy,^[24] as well as highly anisotropic charge transport properties.^[23] Besides, unlike 3D ABX_3 perovskites, 2D layered perovskites offer the possibility to finely tune their physical properties by functionalizing the organic moiety with photo-active molecules.^[25] Last but not least, 2D HOIPs are characterized by weak hydrogen-like and van-der-Waals interlayer bounds, granting remarkable mechanical flexibility even in the form of centimetre-scale single crystals.^[26]

2D HOIPs possess several attractive assets as active layer in direct X-ray detection. Dark current is a key figure of merit for X-ray detectors that affect the signal/noise ratio and limit of detection (LoD) of the device. 2D HOIPs-based detectors display dark current levels 3 orders of magnitude lower than 3D HOIPs-based devices.^[23,27,28] Noteworthy, the transport properties of 2D HOIPs in the direction parallel to the inorganic sheets are similar to that of 3D HOIPs, with for instance identical electron and hole effective masses.^[29,30] The high resistivity of 2D HOIPs has thus been attributed to a lower intrinsic charge carrier density, due to lower unintentional self-doping.^[29] Finally, ion migration phenomena are considered to be one of the main cause for dark current drift observed in 3D HOIP devices, limiting their stability under continuously applied bias. Thanks to the stronger hydrogen bonding provided by the cation $R-NH_3^+$, ion migration is suppressed in 2D HOIPs.^[31]

Despite these interesting and promising properties, only very recently a few X-ray detectors featuring low dimensional

perovskites have been reported.^[28,32,33] Besides, only one included $n = 3$ bromide-based low dimensional perovskite ($C_4H_9NH_3)_2(C_2H_5NH_3)_2Pb_3Br_{10}$ single crystals.^[33] Yet, I^- substitution with Br^- is expected to provide better X-ray absorbers, as it will help reducing to intrinsic charge carrier density due to enlarged band gap.^[34] Additionally, bromide-based HOIPs are less prone to oxidation by environmental O_2 .^[35] All the above consideration, combined with the absence of defects linked to A site cations in $n = 1$ perovskites^[29,31] made us consider the 2D layered perovskite PEA_2PbBr_4 ($PEA = C_6H_5C_2H_4NH_3^+$) as a material with high potentialities as X-ray direct detectors. For the first time, we demonstrate the excellent performance as X-ray direct detectors of 2D HOIP micro-crystalline films directly deposited from solution onto pixelated flexible substrates compatible with large-area deposition techniques and ready for scalability. The tested devices are 2-terminal photoconductors that show exceptionally low dark current for a non-diode structure (10^{-13} A at 500 V mm^{-1} electric field), without the necessity of interlayers. The optimal electrical contact between the crystal grains and the electrodes is witnessed by the exceptionally fast response/decay times ($147/768\text{ ns}$) assessed under UV light. We measured the device performances as X-ray dosimeter (at 40 and 150 kVp accelerating voltages), achieving very good sensitivity up to $806\text{ }\mu\text{C Gy}^{-1}\text{ cm}^{-2}$ and excellent LoD of $42 \pm 4\text{ nGy s}^{-1}$. Noteworthy, the micro-crystalline PEA_2PbBr_4 films display remarkably stable response under constant bias and irradiation, with negligible dark current drift and suppressed ion migration, above continuous pulsed X-ray exposition for 30 min at 80 V, even after 80 days from fabrication. This constitutes the highest level of operational stability achieved for X-ray detectors based on thin films, and competes with detectors based on high-quality single crystals.^[28,36] These results demonstrate that bromide-based $n = 1$ PEA_2PbBr_4 perovskite directly deposited from solution onto a flexible plastic substrate form a robust and reliable electrical contact with the bottom patterned electrodes, opening the way for reliable, large-area, flexible, and ultra-fast X-ray detectors industrially scalable with outstanding efficiency/cost ratio.

2. Results and Discussion

We fabricated 2-terminal devices, based on PEA_2PbBr_4 polycrystalline films directly deposited by spin-coating on a pixelated flexible substrate. Polyethylene terephthalate (PET) substrates ($125\text{ }\mu\text{m}$) were patterned with interdigitated Cr/Au electrodes using photolithography (see Experimental Section). The final devices resulted in a linear array of pixelated photoconductors in bottom-electrode configuration (Figure 1a). We have developed a fast and efficient fabrication method such that the whole fabrication process could be performed within one day. The spin-coated PEA_2PbBr_4 films were composed by large crystal grains, with an average thickness of $1.9 \pm 0.8\text{ }\mu\text{m}$ and average size of $33.5 \pm 8.3\text{ }\mu\text{m}$ (see Figure S1, Supporting Information). Usually, such large grain size in low-dimensional perovskite films results from complex synthesis process, using techniques such as hot-casting^[37] or solvent engineering.^[38] Instead, the choice of PEA_2PbBr_4 material enables the use of single-step spin-coating process and offers high-quality films

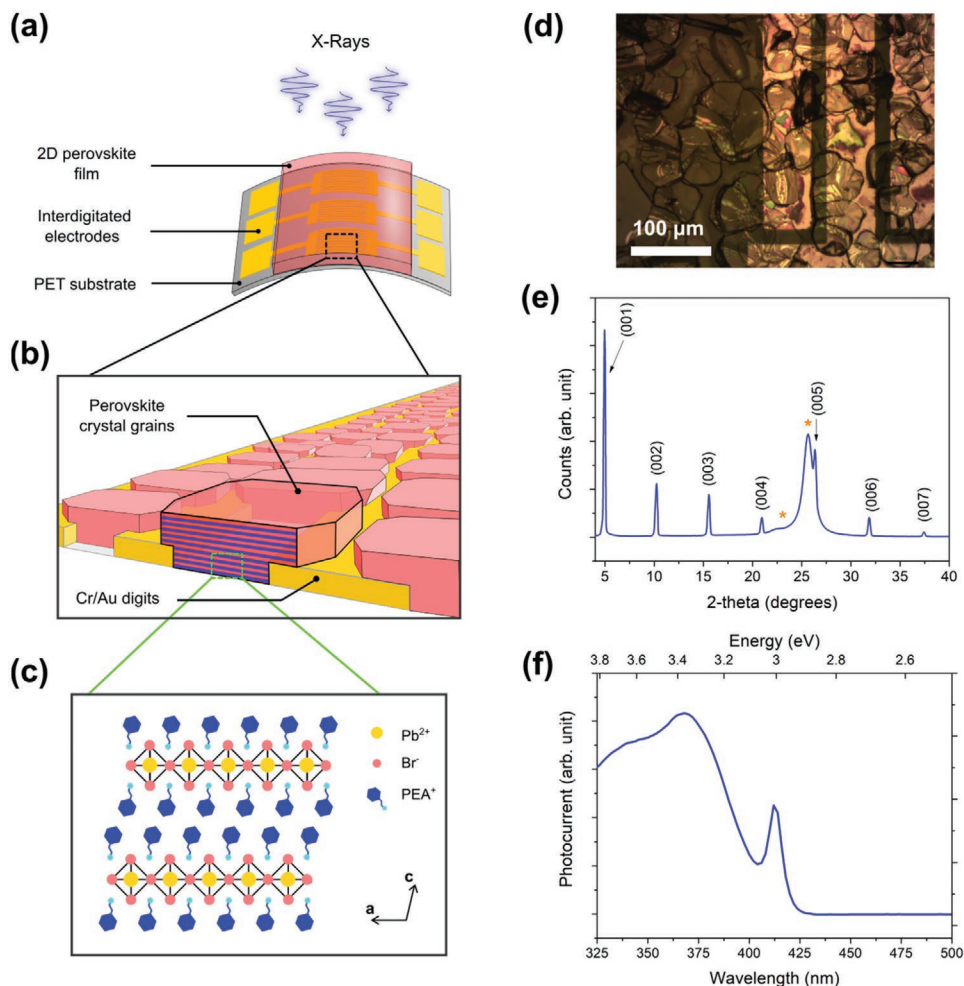


Figure 1. 2D HOIP micro-crystalline films photoconductor fabrication. a–c) Graphical representation of the device. a) Schematic of the 2-terminal pixelated device fabricated on flexible PET substrate. b) Illustration of the 2D perovskite film morphology. c) Schematic of the $\text{PEA}_2\text{PbBr}_4$ crystal structure projected along the direction $\langle 010 \rangle$ showing the stacking of the 2D layers. d) Microscope image showing the film morphology close to the pixel area. e) XRD pattern of the $\text{PEA}_2\text{PbBr}_4$ photoconductor (blue line). The orange asterisks display the reflections from the underlying PET substrate. f) Photocurrent spectrum (blue line) of the $\text{PEA}_2\text{PbBr}_4$ thin film photoconductor biased at 10 V.

even on patterned metal electrodes (see Figure S2, Supporting Information). In fact, the tendency of $\text{PEA}_2\text{PbBr}_4$ to form highly crystalline films with large grains was already noted by Xie et al. on glass substrates.^[39] It is interesting to note that the crystal grains grow preferentially in-between the channel with an average grain size larger than the channel length (20 μm). In this geometry, the crystal grains form a conductive bridge between the electrodes, which implies that the charge conduction from the positive electrode to the negative electrode mainly occurs in a single crystal-like grain (Figure 1b,d). X-ray diffraction (XRD) analyses confirm the nature and crystallinity of the perovskite material. The thin film XRD pattern of the device shown in Figure 1e displays a series of sharp and intense periodic reflections, as well as a broad peak around 25° which is attributed to the PET substrate. The peaks were assigned to the (00*l*) (*l* = 1,2,3,...) family of planes using the crystal data provided in ref. [39,40]. The crystal structure is monoclinic and belongs to the space group $P-1$.^[40] As it is usually observed in 2D layered perovskites, $\text{PEA}_2\text{PbBr}_4$ thin films grow preferentially

with the in-plane direction parallel to the substrate, showing only the (00*l*) planes corresponding to the stacking of the layers in a standard Θ - 2Θ scan.^[41] The photocurrent (PC) spectrum of a $\text{PEA}_2\text{PbBr}_4$ thin film shown in Figure 1f exhibits a narrow peak located at 412 nm, as well as a broad band at lower wavelength. We identified the narrow peak as the 1s Wannier exciton transition from the $[\text{PbBr}_6]$ inorganic sheets, followed by the exciton Rydberg series (2s, 3s, etc...) and continuum states.^[24] The maximum of the exciton peak is red-shifted by ≈ 8 nm with respect to the absorbance spectra reported in previous works.^[42,43] The red-shift of the exciton can be understood by absorption effects based on the Beer-Lambert model $I(\lambda, d) = I_0(\lambda) e^{-\alpha_l d}$ with $I(\lambda, d)$ the light intensity at the distance *d* from the impinging surface, $I_0(\lambda)$ the incident light intensity and α_l the absorption coefficient. We assume that, due to limited interlayer charge transport in the out-of-plane direction, the photogenerated charges are mainly collected at the bottom of the crystalline grains, near the bottom electrodes. At higher wavelength, the light penetration depth is larger, possibly resulting in the red

shift observed in the photogenerated current spectrum. It is interesting to point out that PC is effectively generated even with excitation in the lower λ (350–400 nm) region, where α_λ is in the range 10^4 – 10^5 cm^{-1} and the penetration depth is below 500 nm.^[43] This implies that an important fraction of photogenerated charges are effectively transported from the top to the bottom of the crystalline grains. The possible mechanisms responsible for this long range (>1 μm) transport in $\text{PEA}_2\text{PbBr}_4$ will be discussed below.

The I – V characteristics of micro-crystalline $\text{PEA}_2\text{PbBr}_4$ films in the dark and under UV illumination (380 nm UV-light LED) are shown in Figure 2a. The dark current measured during this experiment is extremely low (2×10^{-13} A at 10 V) corresponding to the value obtained by Zhang et al. with $\text{PEA}_2\text{PbBr}_4$ single crystals,^[27] and one order of magnitude lower than for ultra-high quality PEA_2PbI_4 single crystals^[23] at comparable electric field. As shown by Peng et al., the ultra-low dark current in 2D perovskites originates from low charge carrier densities due to low self-doping by intrinsic defects.^[29] Under increasing illumination with light irradiance ranging from 2×10^{-4} to 0.6 mW cm^{-2} , the PC rises and shows an $I_{\text{ON}}/I_{\text{OFF}}$ ratio as high as 10^4 . This value is comparable to that of $\text{PEA}_2\text{PbBr}_4$ single crystals^[27] and indicates an efficient charge collection process. This demonstrates both the high quality of the here presented $n = 1$ 2D perovskite micro-crystalline films, that exhibit charge transport properties close to single crystal ones, and the good electrical contact with the bottom interdigitated electrodes. The figures of merit used to assess the capacity of the device to detect light are the responsivity $R = \frac{I_{\text{PC}}}{P_0 A}$ and the specific detectivity $D^* = \frac{R \sqrt{A}}{i_n}$ with I_{PC} the PC, P_0 the incoming light intensity (light irradiance), A the effective illumination area, and i_n the noise current (Figure 2b). The noise current of the $\text{PEA}_2\text{PbBr}_4$ micro-crystalline devices ($i_n = 1.29 \times 10^{-16}$ A $\text{Hz}^{-1/2}$) is three orders of magnitude lower than in $\text{CH}_3\text{NH}_3\text{PbBr}_3$ and $\text{CH}_3\text{NH}_3\text{PbI}_3$ single crystal photodetectors.^[23,27] Further details on the estimation of the noise current are provided in the Experimental Section section. The low noise of our devices could be an indication of low trap densities, enabled by the lack of defects related to A-site cations.^[29] The responsivity R of the $\text{PEA}_2\text{PbBr}_4$ micro-crystalline photodetectors, up to 8.26 mA W^{-1} at 10 V applied bias, is comparable to those of $\text{PEA}_2\text{PbBr}_4$ single crystal photodetector reported by Zhang et al., while the D^* values are typically one order of magnitude lower.^[27] Both responsivity R and specific detectivity D^* tend to increase at lower light irradiance, with a plateau below 10^{-3} mW cm^{-2} . The R and D^* plateau coincides with a change of regime in the PC as a function of light intensity (see Figure S3, Supporting Information). In the low light intensity region (10^{-4} – 10^{-3} mW cm^{-2}), the PC scales with the light intensity following the power law $\propto P_0^\alpha$ with $\alpha = 0.86$, while in the high light intensity region (10^{-3} – 10^1 mW cm^{-2}) the PC scales following $\propto P_0^\alpha$ with $\alpha = 0.68$. The decrease in α with increasing light intensity might be correlated to the occurrence of many-body interactions.^[29] In fact, exciton-exciton annihilation was found to be effective in iodide-based low dimensional perovskites $(\text{PEA})_2(\text{MA})_{n-1}\text{Pb}_n\text{I}_{3n+1}$.^[44] We thus assume that the steep decrease in R , D^* , and α at light intensity $\approx 10^{-3}$ mW cm^{-2} is due to the emergence of exciton-exciton annihilation which limits the carrier injection at high light intensity.

Noteworthy, the penetration depth of the light was estimated to be only 500 nm at the LED probe wavelength (380 nm). The PC measured in Figure 1c and the high responsivity R and D^* extracted from Figure 2b thus imply long range (>1 μm) carrier transport from the top part of the crystal to the bottom

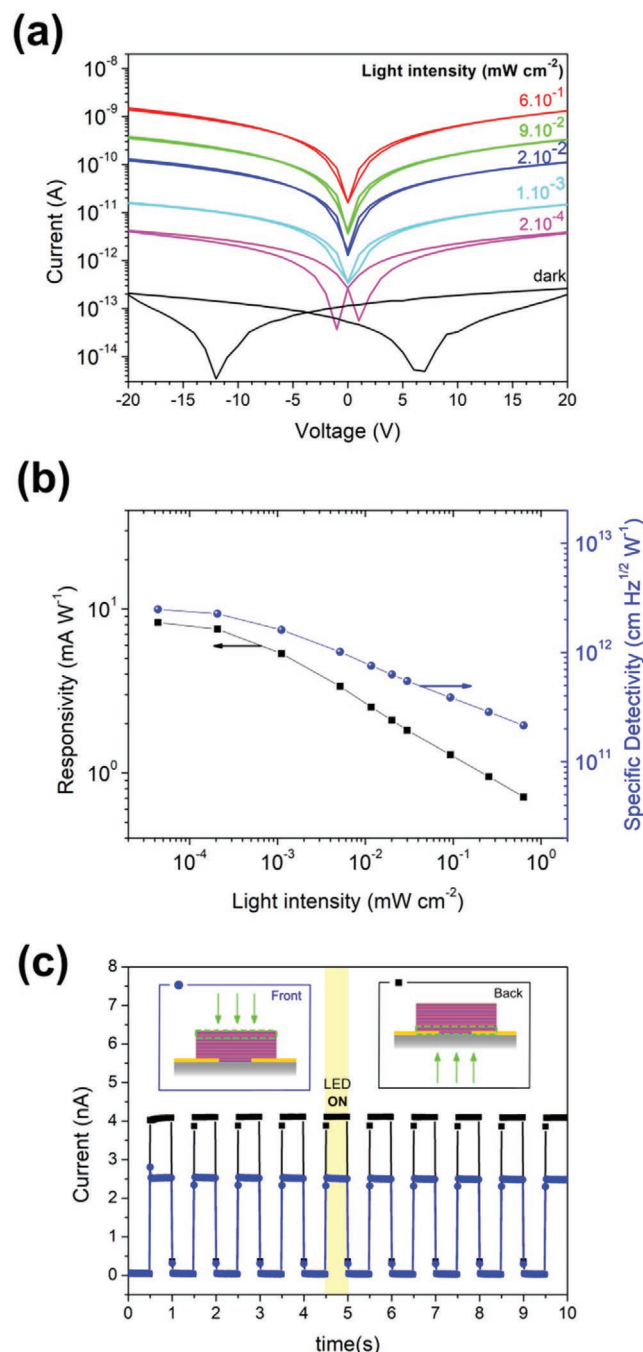


Figure 2. Device characterization under UV light. a) Photoconductivity experiment performed under a 380 nm UV-light LED at different light intensity. b) Responsivity (black) and specific detectivity (blue) as a function of light intensity for the micro-crystalline $\text{PEA}_2\text{PbBr}_4$ device operated at 10 V. c) Dynamic current response of the device operated at 10 V under 380 nm UV light in front illumination (blue) and back illumination (black) configuration.

electrodes. To appreciate the contribution of the out-of-plane transport, we compared the PC generated by illuminating the devices from the front (light from the surface opposite to the metal electrodes) and from the back (light through the transparent substrate and from the same surface of the metal electrodes). Figure 2c shows that the PC is only $\approx 37\%$ smaller when the device is illuminated from the top surface, with respect to that when the device is illuminated from the bottom surface. Considering that a negligible fraction ($10^{-8}\%$) of the incident light should reach the buried electrodes when the device is illuminated from the top, and the poor charge transport in the out-of-plane direction, we would expect negligible to no signal in this configuration. On the contrary, this experiment shows that sizeable transport of photo-generated charges occurs from the top to the bottom of the crystals. The charge transport could be mediated through i) charge carrier diffusion in the direction parallel to the planar electrodes, that is in the out-of-plane direction with respect to the inorganic PbBr_6 layers or ii) photon transport through the volume of the crystal grains and photon recycling processes. On the one hand, it is known that 2D layered perovskites materials such as $\text{PEA}_2\text{PbBr}_4$ exhibit reduced charge carrier transport in the out-of-plane direction due to the presence of the interlayer spacers which act as barriers for both electron and holes.^[45] However several 2D perovskites-based photodetectors were reported to provide reasonably good PCs even in sandwiched electrode geometry.^[23,46] In addition, photon recycling was found recently to be efficient in the 2D layered perovskite BA_2PbI_4 ($\text{BA} = \text{C}_4\text{H}_9\text{NH}_3^+$).^[47] Photon recycling is a light-mediated energy transport process in which charge carriers diffuse through the material via multiple absorption/re-emission events. Photon recycling demands high absorption coefficient and refractive index, small Stokes shifts, and large internal photoluminescence quantum yield (PLQY). All these requirements are met in $\text{PEA}_2\text{PbBr}_4$, and PLQY as high as 79% has been reported for this material.^[42,47–49] We believe that the photon recycling process could explain the good performances of the here presented photodetectors under UV-light despite limited out-of-plane charge carrier diffusion.

We investigated the time response of the 2D $\text{PEA}_2\text{PbBr}_4$ micro-crystalline thin film devices under picosecond UV-laser excitation with ultra-fast readout electronics (see Experimental Section).^[23] Figure 3a displays a typical response of the devices to laser excitation, with a well-defined box-like response

that scales with the laser excitation intensity (see Figure, in Supporting Information). We define τ_{rise} and τ_{fall} as the time interval needed to increase the PC from 10% to 90% of its maximum value (respectively decrease from 90% to 10%). The average τ_{rise} and τ_{fall} values were found to be 147 ± 10 and 768 ± 109 ns respectively, which is more than 5 orders of magnitude faster than thin film photodetectors based on $\text{Cs}_{0.05}(\text{FA}_{0.83}\text{MA}_{0.17})_{0.95}\text{PbI}_{3-x}\text{Br}_x$ ^[12] and CsPbBr_3 .^[14] Zhang et al.^[27] measured fast τ_{rise} and τ_{fall} values of 0.41 and 0.31 ms respectively for a UV-photodetector based on $\text{PEA}_2\text{PbBr}_4$ single crystal,^[27] while Tsai et al. measured ultra-fast $\tau_{\text{rise}} < 500$ ns and fast $\tau_{\text{fall}} = 20\text{--}60$ μs under UV-light for a thin film detector based on the RP perovskite $(\text{BA})_2(\text{MA})_2\text{Pb}_3\text{I}_{10}$.^[32] The ultra-fast response time of the here presented $\text{PEA}_2\text{PbBr}_4$ micro-crystalline devices surpasses state-of-the-art photodetector materials (e.g., Se, ZnO, TiO_2 , graphene)^[50,51] and most perovskites materials.^[32,35] In fact, to the best of our knowledge, only MAPbI_3 -Organic bulk heterojunctions exhibit faster response times.^[52,53] Interestingly, the fall time of our device is up to 100 times faster than the one found for thin film photodiodes based on $(\text{BA})_2(\text{MA})_2\text{Pb}_3\text{I}_{10}$.^[32] Electrically active traps contribute to the increase of the fall time by the means of long charge de-trapping. We suggest that the ultra-fast response of the $\text{PEA}_2\text{PbBr}_4$ micro-crystalline devices can be attributed to various factors: i) a reduced trap state density in bromide-based 2D perovskites with respect to iodide-based 2D perovskites; ii) the $n = 1$ crystal structure, likely to further enhance the time response by its intrinsic lower density of shallow traps linked to, for example, A site cation vacancies;^[31] iii) optimal contact with the bottom electrodes that do not produce additional trap states at the perovskite–metal interface.

The linear attenuation coefficients of $\text{PEA}_2\text{PbBr}_4$ and of some other benchmark materials used for ionizing radiation detection are shown in Figure 4a. For both soft and hard X-rays, the linear attenuation coefficient of $\text{PEA}_2\text{PbBr}_4$ is comparable to CdTe and $\text{CH}_3\text{NH}_3\text{PbBr}_3$ and on average one order of magnitude higher than commercially available silicon. The attenuated fraction values for 40 and 150 kVp accelerating voltages are 4% and 0.4% respectively, calculated for a 2 μm -thick $\text{PEA}_2\text{PbBr}_4$ layer. Indeed, this film thickness does not provide sufficient attenuation to fully absorb the incident photons, but it was chosen as a trade-off between X-ray absorption and mechanical flexibility. Besides, previous works have shown that thin

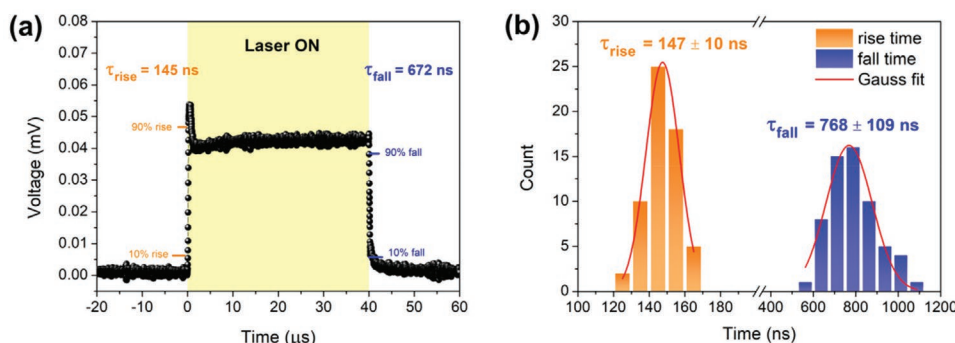


Figure 3. Time response under UV laser excitation. a) Time response of the device biased at 9 V excited with a 380 nm UV laser. The duration of the laser burst is 40 μs and Laser optical power is 5 mW. b) Frequency counts of the rise time τ_{rise} and fall time τ_{fall} for several ON/OFF pulses. The red line depicts the Gaussian fit of the distribution.

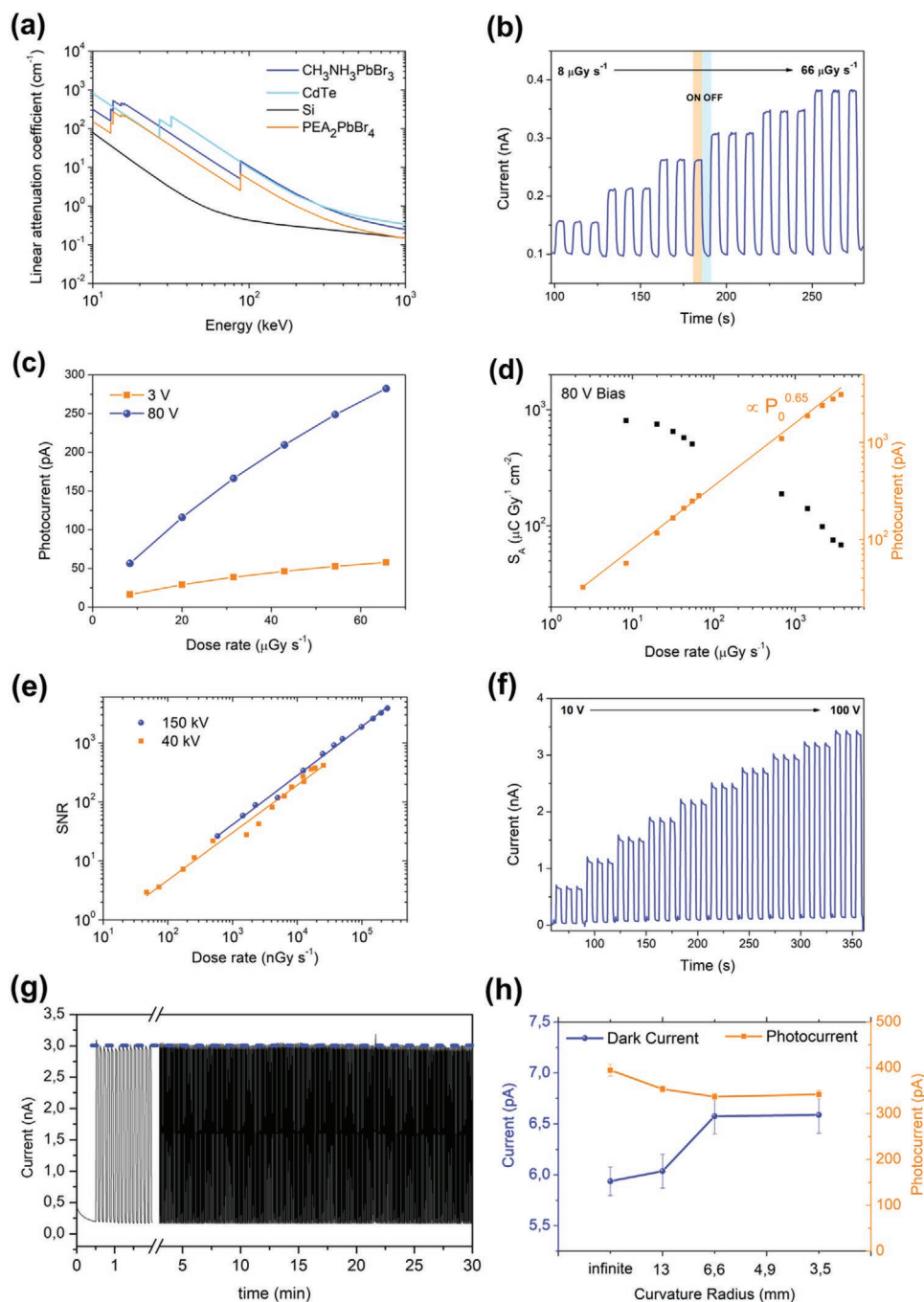


Figure 4. Electrical response to X-rays. a) Linear attenuation coefficient of $\text{PEA}_2\text{PbBr}_4$, $\text{CH}_3\text{NH}_3\text{PbBr}_3$, CdTe , and Si as a function of photon energy. b) Dynamic X-rays response under X-rays with 150 kVp accelerating voltage (80 V bias). c) X-ray induced PC as a function of the dose rate at 3 V (orange) and 80 V (blue) applied bias. d) Sensitivity per unit area S_A (black) and PC (orange) as a function of the dose rate. The sensitivity is calculated as the first derivative of the PC with respect to the dose rate and it is normalized by the total pixel area (0.63 mm^2). e) SNR as a function of the dose rate for 150 kVp (blue) and 40 kVp (orange) accelerating voltages. f) Dynamic X-rays response at 150 kVp and bias increasing from 10 to 100 V. Each step corresponds to a 10 V bias increase. g) Stability of the dynamic response to X-rays at a constant 80 V applied bias after 80 days of aging. The dose rate and the total dose received are 4.2 mGy s^{-1} and 3.8 Gy respectively, over 300 pulses. h) Dark current (blue) and PC (orange) as a function of the curvature radius of the device biased at 5 V under X-rays with 40 kVp accelerating voltage and dose rate 3.6 mGy s^{-1} .

(sub-micrometer) 2D and 3D perovskite films are suitable for X-ray dosimetry despite low X-ray attenuation.^[14,32] Figure 4b shows the dynamic response of the measured PC under X-rays at 150 kVp with dose rates ranging from 8 to $66 \mu\text{Gy s}^{-1}$ and

80 V applied bias. It is worth noticing that the devices were irradiated from the front, although we do not expect significant differences in the collected signal when illuminating from the back due to the high penetration of X-rays and the negligible

absorption of the plastic substrate. The current exhibits a fast box-like response to X-rays, in accordance with the ultra-fast response under UV laser (Figure 3a). The X-rays induced PC, defined as $\Delta I = I_{\text{ON}} - I_{\text{OFF}}$, sizably scales with increasing bias, while the dark current remains low below 10^{-10} A even at large applied bias (>100 V), as seen in Figure S5, Supporting Information. The devices exhibit an optimized PC-to-dark current ratio $\Delta I/I_{\text{OFF}}$ at applied bias of 80 V, even if they can reliably operate already at very low bias of 3 V (see Figure S6, Supporting Information). The PC as a function of the dose rate follows a power law $\propto P_0\alpha$ with $\alpha = 0.65$ and $P_0 =$ dose rate (Figure 4d). The exponent is comparable to that obtained under UV-light excitation (see Figure S3, Supporting Information), however, under X-rays no change of exponent with increasing dose rate was observed. This can be due to the higher density of excitons generated under X-rays, that trigger exciton–exciton annihilation process even at low radiation flux.^[44]

We calculated the sensitivity S_A as the first derivative of the PC (ΔI) versus dose rate (D.R.), $S_A = \frac{1}{A} \frac{\partial \Delta I}{\partial \text{D.R.}}$ with A the total pixel area (0.63 mm^2). The sensitivity reaches values up to $806 \pm 6 \mu\text{C Gy}^{-1} \text{ cm}^{-2}$ under X-rays at 150 kVp, with an applied bias of 80 V and dose rates in the range (8–100) $\mu\text{Gy s}^{-1}$ (Figure 4d), which is at least one orders of magnitude higher than α -Se detectors and higher than thin film low-dimensional perovskite detectors based on $(\text{C}_4\text{H}_9\text{NH}_3)_2(\text{CH}_3\text{NH}_3)_2\text{Pb}_3\text{I}_{10}$.^[18,32,54] The very good sensitivity values are supported by the mobility-lifetime product $\mu\tau = 1.09 \pm 0.07 \times 10^{-5} \text{ cm}^2 \text{ V}^{-1}$ estimated from the PC generated in a $\text{PEA}_2\text{PbBr}_4$ micro-crystalline lateral photoconductor under UV light (see Figure S7, Supporting Information). This $\mu\tau$ value is comparable to that obtained for a $\text{PEA}_2\text{PbBr}_4$ single crystal^[27] and larger than that of α -Se,^[54] thus assessing the good transport properties of the material. In order to evaluate the lowest detectable dose rate, the signal-to-noise ratio (SNR) was plotted as function of dose rate (Figure 4e). The ultra-low noise current of the device offers an SNR as high as 10^2 at a dose rate of $2 \mu\text{Gy s}^{-1}$, which is a typical value in medical X-ray mammography ($5.5 \mu\text{Gy s}^{-1}$).^[55] Following the IUPAC standard, the LoD was linearly extrapolated from the plot presented in Figure 4e, and defined as the dose rate at which the SNR reaches a value of 3. Using this method, we obtained a LoD of $57 \pm 7 \text{ nGy s}^{-1}$ for X-rays at 40 kVp, and $42 \pm 4 \text{ nGy s}^{-1}$ at 150 kVp. The latter value is the lowest achieved for perovskite thin film detectors^[12,13,16,32] and is even comparable to the values obtained for high-quality perovskite single crystals.^[17,18] In fact, to the best of our knowledge, the only superior LoD was found for a 0D perovskite $\text{MA}_3\text{Bi}_2\text{I}_9$ single crystal with a value of 0.62 nGy s^{-1} .^[56] This excellent LoD is notably permitted by the exceptionally low dark current that grants a signal-to-noise-ratio suitable to detect such a small dose rate (see Figure S8, Supporting Information).

The here reported $\text{PEA}_2\text{PbBr}_4$ micro-crystalline devices are exceptionally stable under long-term operation and exhibit no signs of drifting or bias stress under increasing bias, as shown in Figure 4f,g. The PC remains perfectly stable throughout 30 min of continuously pulsed exposure to X-rays at 150 kVp, with high dose rate of 4.2 mGy s^{-1} and a high applied bias of 80 V (total received dose about 3.8 Gy). Notably, the measurement shown in Figure 4g was performed 80 days after the fabrication of the device, which was stored in a box at room

temperature and mild humidity $\approx 20\%$ RH. Comparable stability under operation has only been reported for top-quality 2D perovskite^[28] or triple-cation single crystals,^[36] and this assesses the excellent quality of the micro-crystal grains and stability of the contacts even with high externally applied bias. The drift of the dark current was found to be exceptionally low with a negligible $I_{\text{drift}} = 6.8 \times 10^{-15} \text{ nA cm}^{-1} \text{ s}^{-1} \text{ V}^{-1}$, several orders of magnitude below the one measured in single crystal detectors based on $\text{F-PEA}_2\text{PbI}_4$.^[28] The excellent stability of the signal is further confirmed even after continuous X-ray exposure for 10 min and the perfect overlap of the IV characteristic before and after the prolonged stability test (Figure S9, Supporting Information). The reduced dark current drift can be assigned to the substitution of iodine atoms with bromide atoms, that was found to decrease by eightfold the fraction of migrating ionic species in $\text{CH}_3\text{NH}_3\text{PbX}_3$ perovskites.^[57] In addition, dark current instability in $\text{CH}_3\text{NH}_3\text{PbBr}_3$ was recently attributed to electrochemical reactions at the interface with the electrodes. Those reactions leading to the formation of metal-halide compounds could be favored by migration of halide vacancies.^[58] The superior operational stability of the $\text{PEA}_2\text{PbBr}_4$ micro-crystalline device could thus be attributed to suppressed ionic species (bromide atoms and/or vacancies) migration phenomena that increases the resilience of the material to aging-induced defects. In order to experimentally prove and assess the flexibility of the detectors, we monitor the dark current and the X-ray induced PC under bending with decreasing substrate curvature radii (increasing strain on active layer), from infinite (flat) to 3.5 mm. Figure 4h shows that for radii smaller than 6.6 mm occurs an increase of dark current and a reduction of the PC. The deviations are small (about 10%) and they are stable down to radius of 3.5 mm (about the curvature of the hand little finger). Figure S10, Supporting Information, confirms that the small degradation is permanent, as the electrical properties remain stable once the device is restored to flat condition and also to multiple bending cycles of the same radius. This conditioning effect is well known in flexible electronic systems, and it has been associated with modifications generated at the nanoscale in polycrystalline layer during the bending, like small cracks or delamination at the interface.^[59,60]

3. Conclusion

The present study demonstrates the excellent properties of pixelated X-ray direct detector based on thin films of 2D layered $n = 1$ perovskite $\text{PEA}_2\text{PbBr}_4$. The fabricated devices are arrays of 2-terminal planar photoconductor pixels with micro-crystalline films of perovskite directly deposited on top of the electrodes via solution process at low temperature (70°C), enabling the use of flexible PET substrates and ready for up-scalability. The grains that compose the perovskite films exhibit high crystallinity and provide an optimal electrical contact with the electrodes, both in terms of carrier collection and stability. The analysis of the electrical response under UV light showed that the $\text{PEA}_2\text{PbBr}_4$ detectors display faster response/decay times than previous 2D HOIP based detectors, and surpasses that of state-of-the-art solid-state photodetector materials (e.g., α -Se, ZnO, TiO_2 , graphene). The performances of the devices as ionizing radiation

detectors were evaluated under X-rays up to 150 kVp. Good sensitivity up to $806 \pm 6 \mu\text{C Gy}^{-1} \text{cm}^{-2}$ and an LoD down to $42 \pm 4 \text{ nGy s}^{-1}$ were measured, the latter value being the lowest for thin film direct X-ray detectors. Notably, the crystal-like films directly grown on electrodes exhibit a remarkable stability under constant applied bias and irradiation, which is only matched by the highest-quality perovskite single crystals. This confirms that $\text{PEA}_2\text{PbBr}_4$ micro-crystalline films are very efficient X-ray absorbers, providing sensitive and robust detection of X-rays. We believe that 2D layered perovskites are ground-breaking materials for the detection of radiations and open the way for lightweight and flexible applications.

4. Experimental Section

Perovskite Material Synthesis: $\text{C}_6\text{H}_5\text{C}_2\text{H}_4\text{NH}_3\text{Br}$ (PEABr, Sigma-Aldrich >98%) and PbBr_2 (Sigma-Aldrich >98%) were mixed in *N,N*-dimethylformamide (DMF, Sigma-Aldrich 99.8% anhydrous) to prepare a 1 M solution with 2:1 molar ratio. The solution was mixed thoroughly for 5 h until complete dissolution of the precursors and filtrated through a $0.22 \mu\text{m}$ PTFE filter prior to use.

Thin Film Pixelated Photoconductor Fabrication: A pixelated Cr/Au interdigitated electrode pattern was fabricated on PET substrates using photolithography. Briefly, a mask was designed on PET substrates ($125 \mu\text{m}$) with S1818 positive photoresist followed by evaporation of $\approx 10 \text{ nm}$ Cr and $\approx 30 \text{ nm}$ Au. The channel in the interdigitated pattern was $W = 7.56 \text{ mm}$ width and $L = 20 \mu\text{m}$ length. After the lift-off of the photoresist, the Cr/Au patterns were sonicated in water for 10 min then cleaned in air plasma for 2 min prior to perovskite deposition. The perovskite material was deposited by spin-coating at 2000 rpm for 60 s, followed by a short annealing at 70°C for 1 min.

Electrical Response Under UV and X-Rays: UV photoconductivity measurements and IV characteristics were acquired using a Keithley 6517A electrometer. The noise current i_n was derived from the rooted mean squared values of the dark current under constantly applied bias $I_{\text{RMS}} = \sqrt{i_n^2 B}$ with B the bandwidth (50 Hz). Electrical response under X-ray was acquired by a Keithley 2614B precision Source/Measure Unit. The devices were placed in a faraday box with a $70 \mu\text{m}$ aluminum window for the X-ray measurement. The radiation source was a Hamamatsu L12161 Microfocus X-ray tube with W target used at 40 kVp and 150 kVp accelerating voltages and filament currents ranging from 10 to 500 μA . A lead mechanical shutter was employed to control the ON/OFF beam switching. The dose rates were previously calibrated by a Barracuda radiation detector (RTI Group).

Transient Response Measurement: Excitation source used for time response measurement was a PicoQuant picosecond laser diode (380 nm, 40 ps pulse duration) with Taiko PDL M1 driver. Using built-in bounce mode, pulses were repeated 4000 times at 100 MHz to obtain a 40 μs laser burst. The light-induced current signal was converted to voltage using a current amplifier (FEMTO DHP-CA-100, Gain 10^5 V A^{-1} , bandwidth 3.5 MHz), then the signal was acquired with a Rohde & Schwarz RTB 2004 oscilloscope. The measured τ_{rise} and τ_{fall} values were obtained for several pixels and different spots.

Supporting Information

Supporting Information is available from the Wiley Online Library or from the author.

Acknowledgements

The authors acknowledge funding from European Community through the POR-FESR "FORTRESS" project, grant no. I38D18000150009

(PG/2018/629121). The authors would like to acknowledge Prof. Luca Pasquini for XRD measurements.

Open access funding provided by Universita di Bologna within the CRUI-CARE Agreement.

Conflict of Interest

The authors declare no conflict of interest.

Data Availability Statement

The data that support the findings of this study are available from the corresponding author upon reasonable request.

Keywords

2D layered perovskites, flexible X-ray detectors, hybrid halide perovskites, limit of detection

Received: July 7, 2021

Revised: September 10, 2021

Published online: October 24, 2021

- [1] A. J. J. M. van Breemen, M. Simon, O. Tournant, S. Shanmugam, J.-L. van der Steen, H. B. Akkerman, A. Kronemeijer, W. Ruetten, R. Raaijmakers, L. Alving, J. Jacobs, P. E. Malinowski, F. De Roose, G. H. Gelinck, *npj Flexible Electron.* **2020**, *4*, 22.
- [2] A. B. de González, S. Darby, *Lancet* **2004**, *363*, 7.
- [3] L. Basirico, A. Ciavatti, T. Cramer, P. Cosseddu, A. Bonfiglio, B. Fraboni, *Nat. Commun.* **2016**, *7*, 13063.
- [4] A. Ciavatti, E. Capria, A. Fraloni-Morgera, G. Tromba, D. Dreossi, P. J. Sellin, P. Cosseddu, A. Bonfiglio, B. Fraboni, *Adv. Mater.* **2015**, *27*, 7213.
- [5] I. Temiño, L. Basirico, I. Fratelli, A. Tamayo, A. Ciavatti, M. Mas-Torrent, B. Fraboni, *Nat. Commun.* **2020**, *11*, 2136.
- [6] L. Basirico, P. Cosseddu, B. Fraboni, A. Bonfiglio, *Thin Solid Films* **2011**, *520*, 1291.
- [7] S. Yakunin, D. N. Dirin, Y. Shynkarenko, V. Morad, I. Cherniukh, O. Nazarenko, D. Kreil, T. Nauser, M. V. Kovalenko, *Nat. Photonics* **2016**, *10*, 585.
- [8] L. Basirico, S. P. Senanayak, A. Ciavatti, M. Abdi-Jalebi, B. Fraboni, H. Sirringhaus, *Adv. Funct. Mater.* **2019**, *29*, 1902346.
- [9] H. Wei, Y. Fang, P. Mulligan, W. Chuirazzi, H.-H. Fang, C. Wang, B. R. Ecker, Y. Gao, M. A. Loi, L. Cao, J. Huang, *Nat. Photonics* **2016**, *10*, 333.
- [10] D. Shi, V. Adinolfi, R. Comin, M. Yuan, E. Alarousu, A. Buin, Y. Chen, S. Hoogland, A. Rothenberger, K. Katsiev, Y. Losovyj, X. Zhang, P. A. Dowben, O. F. Mohammed, E. H. Sargent, O. M. Bakr, *Science* **2015**, *347*, 519.
- [11] H. Wei, D. DeSantis, W. Wei, Y. Deng, D. Guo, T. J. Savenije, L. Cao, J. Huang, *Nat. Mater.* **2017**, *16*, 826.
- [12] S. Demchyshyn, M. Verdi, L. Basirico, A. Ciavatti, B. Hailegnaw, D. Cavalcoli, M. C. Scharber, N. S. Sariciftci, M. Kaltenbrunner, B. Fraboni, *Adv. Sci.* **2020**, 2002586.
- [13] H. Mescher, F. Schackmar, H. Eggers, T. Abzieher, M. Zuber, E. Hamann, T. Baumbach, B. S. Richards, G. Hernandez-Sosa, U. W. Paetzold, U. Lemmer, *ACS Appl. Mater. Interfaces* **2020**, *12*, 15774.
- [14] J. Liu, B. Shabbir, C. Wang, T. Wan, Q. Ou, P. Yu, A. Tadich, X. Jiao, D. Chu, D. Qi, D. Li, R. Kan, Y. Huang, Y. Dong, J. Jasieniak, Y. Zhang, Q. Bao, *Adv. Mater.* **2019**, *31*, 1901644.

- [15] J. Peng, K. Ye, Y. Xu, L. Cui, R. Li, H. Peng, Q. Lin, *Sens. Actuators, A* **2020**, 312, 112132.
- [16] Z. Gou, S. Huanglong, W. Ke, H. Sun, H. Tian, X. Gao, X. Zhu, D. Yang, P. Wangyang, *Phys. Status Solidi RRL* **2019**, 13, 1900094.
- [17] A. Ciavatti, R. Sorrentino, L. Basiricò, B. Passarella, M. Caironi, A. Petrozza, B. Fraboni, *Adv. Funct. Mater.* **2021**, 31, 2009072.
- [18] L. Basiricò, A. Ciavatti, B. Fraboni, *Adv. Mater. Technol.* **2020**, 6, 2000475.
- [19] K. Wang, C. Wu, Y. Hou, D. Yang, S. Priya, *J. Mater. Chem. A* **2019**, 7, 24661.
- [20] W. Wei, Y. Zhang, Q. Xu, H. Wei, Y. Fang, Q. Wang, Y. Deng, T. Li, A. Gruverman, L. Cao, J. Huang, *Nat. Photonics* **2017**, 11, 315.
- [21] X. Wang, D. Zhao, Y. Qiu, Y. Huang, Y. Wu, G. Li, Q. Huang, Q. Khan, A. Nathan, W. Lei, J. Chen, *Phys. Status Solidi RRL* **2018**, 12, 1800380.
- [22] L. N. Quan, D. Ma, Y. Zhao, O. Voznyy, H. Yuan, E. Bladt, J. Pan, F. P. García de Arquer, R. Sabatini, Z. Piontkowski, A.-H. Emwas, P. Todorović, R. Quintero-Bermudez, G. Walters, J. Z. Fan, M. Liu, H. Tan, M. I. Saidaminov, L. Gao, Y. Li, D. H. Anjum, N. Wei, J. Tang, D. W. McCamant, M. B. J. Roeffaers, S. Bals, J. Hofkens, O. M. Bakr, Z.-H. Lu, E. H. Sargent, *Nat. Commun.* **2020**, 11, 170.
- [23] Y. Liu, H. Ye, Y. Zhang, K. Zhao, Z. Yang, Y. Yuan, H. Wu, G. Zhao, Z. Yang, J. Tang, Z. Xu, S. (Frank) Liu, *Matter* **2019**, 1, 465.
- [24] J.-C. Blancon, A. V. Stier, H. Tsai, W. Nie, C. C. Stoumpos, B. Traoré, L. Pedesseau, M. Kepenekian, F. Katsutani, G. T. Noe, J. Kono, S. Tretiak, S. A. Crooker, C. Katan, M. G. Kanatzidis, J. J. Crochet, J. Even, A. D. Mohite, *Nat. Commun.* **2018**, 9, 2254.
- [25] F. Lédée, P. Audebert, G. Trippé-Allard, L. Galmiche, D. Garrot, J. Marrot, J.-S. Lauret, E. Deleporte, C. KATAN, J. Even, C. Quarti, *Mater. Horiz.* **2021**, 8, 1547.
- [26] Y. Liu, Y. Zhang, Z. Yang, H. Ye, J. Feng, Z. Xu, X. Zhang, R. Munir, J. Liu, P. Zuo, Q. Li, M. Hu, L. Meng, K. Wang, D. M. Smilgies, G. Zhao, H. Xu, Z. Yang, A. Amassian, J. Li, K. Zhao, S. F. Liu, *Nat. Commun.* **2018**, 9, 5302.
- [27] Y. Zhang, Y. Liu, Z. Xu, H. Ye, Q. Li, M. Hu, Z. Yang, S. (Frank) Liu, *J. Mater. Chem. C* **2019**, 7, 1584.
- [28] H. Li, J. Song, W. Pan, D. Xu, W. Zhu, H. Wei, B. Yang, *Adv. Mater.* **2020**, 32, 2003790.
- [29] W. Peng, J. Yin, K.-T. Ho, O. Ouellette, M. De Bastiani, B. Murali, O. El Tall, C. Shen, X. Miao, J. Pan, E. Alarousu, J.-H. He, B. S. Ooi, O. F. Mohammed, E. Sargent, O. M. Bakr, *Nano Lett.* **2017**, 17, 4759.
- [30] C. C. Stoumpos, D. H. Cao, D. J. Clark, J. Young, J. M. Rondinelli, J. I. Jang, J. T. Hupp, M. G. Kanatzidis, *Chem. Mater.* **2016**, 28, 2852.
- [31] X. Xiao, J. Dai, Y. Fang, J. Zhao, X. Zheng, S. Tang, P. N. Rudd, X. C. Zeng, J. Huang, *ACS Energy Lett.* **2018**, 3, 684.
- [32] H. Tsai, F. Liu, S. Shrestha, K. Fernando, S. Tretiak, B. Scott, D. T. Vo, J. Strzalka, W. Nie, *Sci. Adv.* **2020**, 6, eaay0815.
- [33] C. Ji, S. Wang, Y. Wang, H. Chen, L. Li, Z. Sun, Y. Sui, S. Wang, J. Luo, *Adv. Funct. Mater.* **2020**, 30, 1905529.
- [34] H. Wei, J. Huang, *Nat. Commun.* **2019**, 10, 1066.
- [35] Y. Liu, Y. Zhang, X. Zhu, Z. Yang, W. Ke, J. Feng, X. Ren, K. Zhao, M. Liu, M. G. Kanatzidis, S. (Frank) Liu, *Sci. Adv.* **2021**, 7, eabc8844.
- [36] Y. Liu, Y. Zhang, X. Zhu, J. Feng, I. Spanopoulos, W. Ke, Y. He, X. Ren, Z. Yang, F. Xiao, K. Zhao, M. Kanatzidis, S. (Frank) Liu, *Adv. Mater.* **2021**, 33, 2006010.
- [37] H. Tsai, W. Nie, J.-C. Blancon, C. C. Stoumpos, R. Asadpour, B. Harutyunyan, A. J. Neukirch, R. Verduzco, J. J. Crochet, S. Tretiak, L. Pedesseau, J. Even, M. A. Alam, G. Gupta, J. Lou, P. M. Ajayan, M. J. Bedzyk, M. G. Kanatzidis, A. D. Mohite, *Nature* **2016**, 536, 312.
- [38] J. Qing, X.-K. Liu, M. Li, F. Liu, Z. Yuan, E. Tiukalova, Z. Yan, M. Duchamp, S. Chen, Y. Wang, S. Bai, J.-M. Liu, H. J. Snaith, C.-S. Lee, T. C. Sum, F. Gao, *Adv. Energy Mater.* **2018**, 8, 1800185.
- [39] A. Xie, C. Hettiarachchi, F. Maddalena, M. E. Witkowski, M. Makowski, W. Drozdowski, A. Arramel, A. T. S. Wee, S. V. Springham, P. Q. Vuong, H. J. Kim, C. Dujardin, P. Coquet, M. D. Birowosuto, C. Dang, *Commun Mater* **2020**, 1, 37.
- [40] K. Shibuya, M. Koshimizu, F. Nishikido, H. Saito, S. Kishimoto, *Acta Cryst. E* **2009**, 65, m1323.
- [41] F. Lédée, G. Trippé-Allard, H. Diab, P. Audebert, D. Garrot, J.-S. Lauret, E. Deleporte, *CrystEngComm* **2017**, 19, 2598.
- [42] D. Liang, Y. Peng, Y. Fu, M. J. Shearer, J. Zhang, J. Zhai, Y. Zhang, R. J. Hamers, T. L. Andrew, S. Jin, *ACS Nano* **2016**, 10, 6897.
- [43] K. Jemli, P. Audebert, L. Galmiche, G. Trippé-Allard, D. Garrot, J.-S. Lauret, E. Deleporte, *ACS Appl. Mater. Interfaces* **2015**, 7, 21763.
- [44] G. Delport, G. Chehade, F. Lédée, H. Diab, C. Milesi-Brault, G. Trippé-Allard, J. Even, J.-S. Lauret, E. Deleporte, D. Garrot, *J. Phys. Chem. Lett.* **2019**, 10, 5153.
- [45] J. Leveille, C. Katan, L. Zhou, A. D. Mohite, J. Even, S. Tretiak, A. Schleife, A. J. Neukirch, *Phys. Rev. Mater.* **2018**, 2, 105406.
- [46] J. V. Passarelli, D. J. Fairfield, N. A. Sather, M. P. Hendricks, H. Sai, C. L. Stern, S. I. Stupp, *J. Am. Chem. Soc.* **2018**, 140, 7313.
- [47] Z. Gan, X. Wen, W. Chen, C. Zhou, S. Yang, G. Cao, K. P. Ghiggino, H. Zhang, B. Jia, *Adv. Energy Mater.* **2019**, 9, 1900185.
- [48] N. Kawano, M. Koshimizu, G. Okada, Y. Fujimoto, N. Kawaguchi, T. Yanagida, K. Asai, *Sci. Rep.* **2017**, 7, 14754.
- [49] X. Gong, O. Voznyy, A. Jain, W. Liu, R. Sabatini, Z. Piontkowski, G. Walters, G. Bappi, S. Nokhrin, O. Bushuyev, M. Yuan, R. Comin, D. McCamant, S. O. Kelley, E. H. Sargent, *Nat. Mater.* **2018**, 17, 550.
- [50] B. Deka Boruah, A. Misra, *ACS Appl. Mater. Interfaces* **2016**, 8, 18182.
- [51] Y. Chang, L. Chen, J. Wang, W. Tian, W. Zhai, B. Wei, *J. Phys. Chem. C* **2019**, 123, 21244.
- [52] L. Shen, Y. Lin, C. Bao, Y. Bai, Y. Deng, M. Wang, T. Li, Y. Lu, A. Gruverman, W. Li, J. Huang, *Mater. Horiz.* **2017**, 4, 242.
- [53] C. Li, H. Wang, F. Wang, T. Li, M. Xu, H. Wang, Z. Wang, X. Zhan, W. Hu, L. Shen, *Light: Sci. Appl.* **2020**, 9, 31.
- [54] M. Z. Kabir, S. Kasap, in *Springer Handbook of Electronic and Photonic Materials* (Eds: S. Kasap, P. Capper), Springer International Publishing, Cham **2017**, pp. 1.
- [55] I. Clairand, J.-M. Bordy, E. Carinou, J. Dures, J. Debroas, M. Denozière, L. Donadille, M. Ginjaume, C. Itié, C. Koukorava, S. Krim, A.-L. Lebacqz, P. Martin, L. Struelens, M. Sans-Merce, F. Vanhavere, *Radiat. Meas.* **2011**, 46, 1252.
- [56] X. Zheng, W. Zhao, P. Wang, H. Tan, M. I. Saidaminov, S. Tie, L. Chen, Y. Peng, J. Long, W.-H. Zhang, *J. Energy Chem.* **2020**, 49, 299.
- [57] L. McGovern, M. H. Futscher, L. A. Muscarella, B. Ehrler, *J. Phys. Chem. Lett.* **2020**, 11, 7127.
- [58] J. Pospisil, A. Guerrero, O. Zmeskal, M. Weiter, J. J. Gallardo, J. Navas, G. Garcia-Belmonte, *Adv. Funct. Mater.* **2019**, 29, 1900881.
- [59] T. Cramer, L. Travaglini, S. Lai, L. Patruno, S. de Miranda, A. Bonfiglio, P. Cosseddu, B. Fraboni, *Sci. Rep.* **2016**, 6, 38203.
- [60] L. Hu, Q. Zhao, S. Huang, J. Zheng, X. Guan, R. Patterson, J. Kim, L. Shi, C.-H. Lin, Q. Lei, D. Chu, W. Tao, S. Cheong, R. D. Tilley, A. W. Y. Ho-Baillie, J. M. Luther, J. Yuan, T. Wu, *Nat. Commun.* **2021**, 12, 466.